nature nanotechnology

Article

https://doi.org/10.1038/s41565-022-01277-z

Efficient electrocatalytic valorization of chlorinated organic water pollutant to ethylene

Received: 15 April 2022

Accepted: 17 October 2022

Published online: 19 December 2022

Check for updates

Chungseok Choi[1,2,7], Xiaoxiong Wang[3,7], Soonho Kwon[4,7], James L. Hart[5], Conor L. Rooney[1,2], Nia J. Harmon[1,2], Quynh P. Sam[5], Judy J. Cha[2,5,6], William A. Goddard III[4] ✉, Menachem Elimelech[3] ✉ & Hailiang Wang[1,2] ✉

Electrochemistry can provide an efficient and sustainable way to treat environmental waters polluted by chlorinated organic compounds. However, the electrochemical valorization of 1,2-dichloroethane (DCA) is currently challenged by the lack of a catalyst that can selectively convert DCA in aqueous solutions into ethylene. Here we report a catalyst comprising cobalt phthalocyanine molecules assembled on multiwalled carbon nanotubes that can electrochemically decompose aqueous DCA with high current and energy efficiencies. Ethylene is produced at high rates with unprecedented ~100% Faradaic efficiency across wide electrode potential and reactant concentration ranges. Kinetic studies and density functional theory calculations reveal that the rate-determining step is the first C–Cl bond breaking, which does not involve protons—a key mechanistic feature that enables cobalt phthalocyanine/carbon nanotube to efficiently catalyse DCA dechlorination and suppress the hydrogen evolution reaction. The nanotubular structure of the catalyst enables us to shape it into a flow-through electrified membrane, which we have used to demonstrate >95% DCA removal from simulated water samples with environmentally relevant DCA and electrolyte concentrations.

1,2-Dichloroethane (DCA) is one of the most widely produced chemicals in the world[1,2]. In the United States alone, ~10 million tons of DCA was produced in 2019 (ref. [3]). Typical industrial uses of DCA are to make medicines, specialty surfactants, functionalized polymers and other fine chemical products[4–7]. During its production and utilization, DCA is released into the environment. In the United States, it was estimated that a total of ~183 tons of DCA was unintentionally discharged into the environment in 2019 (ref. [8]). Unfortunately, DCA is a toxic environmental pollutant. Inhalation or ingestion of DCA can harm critical organs such as the liver, kidneys and lungs, as well as the neurological, cardiovascular and immune systems[1]. The International Agency Research on Cancer has also classified it as possibly carcinogenic to humans[1]. As a result of these health and environmental concerns, the European Union has banned the non-authorized commercial use of DCA despite the heavy reliance of emerging chemistries on DCA as a solvent[4–7], and the US Environmental Protection Agency has set a strict maximum contaminant level of 5 parts per billion for DCA in drinking water[9]. Furthermore, under normal environmental conditions, the

[1]Department of Chemistry, Yale University, New Haven, CT, USA. [2]Energy Sciences Institute, Yale University, West Haven, CT, USA. [3]Department of Chemical and Environmental Engineering, Yale University, New Haven, CT, USA. [4]Materials and Process Simulation Center (MSC), California Institute of Technology, Pasadena, CA, USA. [5]Department of Materials Science and Engineering, Cornell University, Ithaca, NY, USA. [6]Department of Mechanical Engineering and Materials Science, Yale University, West Haven, CT, USA. [7]These authors contributed equally: Chungseok Choi, Xiaoxiong Wang, Soonho Kwon. ✉e-mail: wag@caltech.edu; menachem.elimelech@yale.edu; hailiang.wang@yale.edu

half-life of DCA is approximately 73 days in the vapour phase due to photolysis and as long as 50 years in aqueous solutions due to abiotic hydrolysis, making it a persistent pollutant[1,10].

The conventional way to effectively decompose DCA in an aqueous solution is bioremediation[1]. However, this process is relatively slow in removing DCA pollutants from the environment. The reported half-life of DCA with biodegradation is ~100 days in aerobic water and ~400 days in anaerobic water[11]. In addition, the aerobic bioremediation method oxidizes DCA into CO_2, H_2O and chloride ions (Cl^-) (ref. [12]). This negates the opportunity of harvesting valuable DCA dechlorination products such as ethylene (C_2H_4), which is an essential building block in producing various plastics, solvents and cosmetics[13]. Electrochemical DCA dechlorination, potentially powered by renewable electricity, is a cost-competitive and eco-friendly strategy to remove DCA pollutants and concurrently produce ethylene. Various catalysts have been identified for the electrochemical dechlorination of chlorinated hydrocarbon compounds in aqueous solutions[14–19]. Among them, silver-based catalysts show a remarkable decomposition efficiency (fractional removal after electrochemical treatment) such as 100% for tetrachloroethylene, 1,1,2-trichloroethane or chloroform and Faradaic efficiency (FE) of ~80% for chloroform[18,19]. However, in the case of decomposing DCA contaminants in aqueous solutions, almost all the reported electrocatalysts are limited to less than 50% decomposition efficiency and 50% FE[16–18]. In fact, DCA dechlorination is deemed to be one of the most challenging reactions in the electrochemical decontamination of groundwater because of the persistence of DCA to electrochemical decomposition with increasing water concentration as a result of strong competition from the facile hydrogen evolution reaction (HER)[16,18]. Recent progress in the electrochemical decomposition of DCA was built on non-aqueous electrolytes[20–23]. Nevertheless, high reductive potential (approximately −2.75 V versus the saturated calomel electrode), low reaction rate, low FE (less than 50%) and the inability to handle aqueous solutions remain major problems.

We report here the discovery of the first catalyst that effectively solves all the abovementioned challenges for electrochemical DCA dechlorination. Our catalyst consists of cobalt phthalocyanine (CoPc) molecules supported on multiwalled carbon nanotubes (CNTs), denoted by CoPc/CNT. We show that CoPc/CNT can efficiently convert DCA dissolved in aqueous solutions to ethylene and Cl^-. In 0.1 M $KHCO_3$ with ~87 mM DCA, CoPc/CNT exhibits an onset potential of approximately −0.2 V (all the potentials in this Article are referenced to the reversible hydrogen electrode (RHE), unless otherwise specified) for DCA reduction and an unprecedented ethylene production rate (PR) of ~0.56 mmol g^{-1} s^{-1} at −0.64 V. The FE of ethylene formation is nearly 100% throughout this potential range, with almost no H_2 detected. The high selectivity and activity can be achieved across a wide DCA concentration range and maintained during hours of continuous operation. Kinetic measurements show that the rate-determining step (RDS) is the first dechlorination without protons involved, which is confirmed by density functional theory (DFT) calculations. Incorporating the CoPc/CNT catalyst into an electrified membrane allows us to demonstrate water treatment in an application-relevant flow-through mode. Using simulated water samples with environmentally relevant DCA concentrations, our reactor can realize >95% DCA removal.

CoPc/CNT hybrid material

We prepared the CoPc/CNT hybrid catalyst (Fig. 1a) by supporting CoPc molecules on CNTs via non-covalent π−π interactions following our prior work[24,25]. The CNTs, which can be produced in high purity with a reasonable cost[26], allows effective loading and uniform dispersion of CoPc molecules on the highly conductive surface. Inductively coupled plasma mass spectrometry (ICP-MS) measured ~2.6 wt% CoPc in the hybrid material, corresponding to ~10 μg cm^{-2} CoPc on the CoPc/CNT working electrode. The cyclic voltammogram of CoPc/CNT shows a prominent redox feature of CoPc (Fig. 1b), which indicates that CoPc molecules are effectively anchored on the CNT surface[25]. Integrating the oxidation peak gives an electrochemically active (EA) CoPc loading of ~4.3 μg cm^{-2}, which is approximately 43% of the total CoPc loading measured by ICP-MS, consistent with our prior work[27]. The high EA percentage reflects the molecular-level dispersion of CoPc on the CNT surface, which was characterized by energy-dispersive X-ray (EDX) mapping in our prior work[24,25]. Raman spectroscopic characterization also detects CoPc in the hybrid material (Fig. 1c). Interestingly, compared with unsupported CoPc, supported CoPc exhibits weaker or disappeared vibrational peaks in the <1,000 cm^{-1} region, which could be due to the electronic interaction between CoPc and CNT (ref. [28]). High-resolution scanning transmission electron microscopy (STEM) high-angle annular dark-field (HAADF) imaging of CoPc/CNT reveals the multilayered graphitic structure of CNT and the presence of heavier metal atoms on its surface (Fig. 1d). EDX analysis supports the presence of elemental Co on CoPc-loaded CNTs (Fig. 1e,f) but not on bare CNTs (Supplementary Fig. 1), confirming the effective loading of CoPc.

Electrocatalytic properties

We studied the catalytic performance of CoPc/CNT for electrochemical DCA dechlorination using a gas-tight H-type cell with Ar-carried DCA vapour continuously flowing into the 0.1 M $KHCO_3$ aqueous electrolyte (corresponding to a saturated DCA concentration of ~87 mM) at room temperature and under atmospheric pressure (Supplementary Fig. 2). The high ionic conductivity and pH-buffering capability of the electrolyte provide a stable condition for electrocatalytic measurements. The CoPc/CNT catalyst was compared with polycrystalline Ag, Fe and Pd electrodes (Supplementary Fig. 3). All these selected metals, known for their catalytic activity for the electrochemical dechlorination of some chlorinated hydrocarbon compounds[16–19], exhibit limited catalytic performance for DCA dechlorination. Both Pd and Fe produce H_2 with ~100% FE at all the studied potentials between −0.44 and −0.84 V (Fig. 2a and Supplementary Fig. 4a,b). The Ag catalyst can convert DCA to ethylene, but with low FE (42%) and partial current density (0.14 mA cm^{-2}) at −0.64 V (Fig. 2a and Supplementary Fig. 4c). This performance is consistent with the literature[18]. In contrast, our CoPc/CNT catalyst shows much higher DCA dechlorination rates with ~100% $FE_{ethylene}$ in the potential range from −0.24 to −0.64 V, with almost no H_2 detected (Fig. 2a and Supplementary Fig. 4d). The catalytic current density can be further enhanced by stirring, which improves the diffusion of DCA in the solution (Supplementary Fig. 5). With stirring at 600 rpm, a current density of ~32 mA cm^{-2} with near-unity FE is achieved at −0.54 V (Fig. 2b and Supplementary Fig. 5), which can be maintained for at least 6 h (Supplementary Fig. 6). ICP-MS detects no leaching of Co into the electrolyte after electrolysis, confirming the structural stability of the catalyst and its safety for potential water treatment applications.

To confirm the active site of the catalyst, we separately measured the catalytic performance of CoPc and CNTs. CoPc shows ~100% $FE_{ethylene}$ at −0.44 and −0.54 V (Supplementary Fig. 7a). However, its current density, despite a much higher mass loading of CoPc, is over 100 times smaller than that of CoPc/CNT. Bare CNTs have no activity for DCA dechlorination in the potential range between −0.4 and −0.8 V (Supplementary Fig. 7b). These results not only suggest that CoPc is the catalytically active component for DCA conversion to ethylene but also reveal the importance of hybridization with CNTs in enhancing the reaction rate. We also measured other metal phthalocyanine molecules hybridized with CNTs for DCA dechlorination. Both FePc/CNT and ZnPc/CNT show substantially lower selectivity and activity than CoPc/CNT (Supplementary Fig. 8), which indicates that the Co centre of CoPc is the active site. As the DCA reduction potential range for CoPc/CNT (from −0.2 to −0.9 V) is between the first and second reduction of CoPc, the active site may be Co(I) under the reaction conditions[29,30].

Under the same stirring condition, our CoPc/CNT catalyst exhibits a turnover frequency (TOF) of 30 s^{-1} and PR of 53 mmol g^{-1} s^{-1} for

https://doi.org/10.1038/s41565-022-01277-z

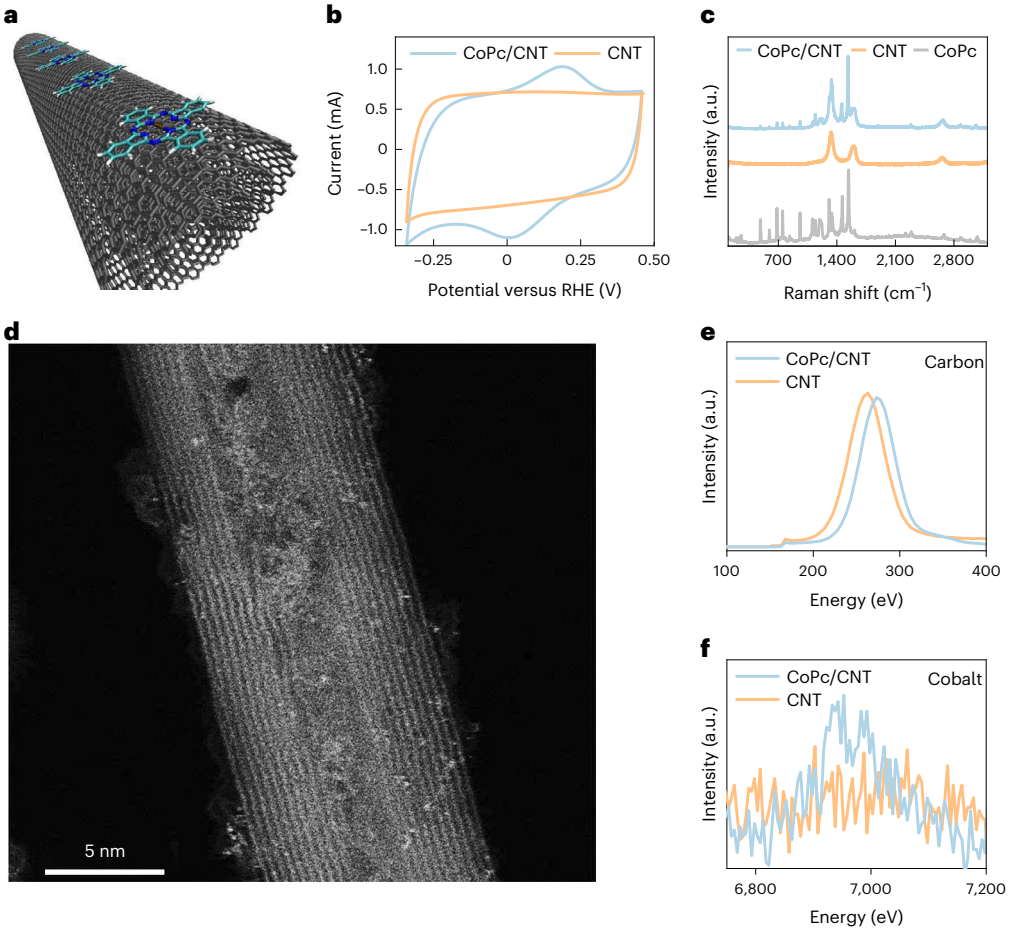

Fig. 1 | CoPc/CNT catalyst. a, Schematic of the CoPc/CNT hybrid structure. **b**, Cyclic voltammograms of CoPc/CNT and CNT measured in 0.1 M aqueous $KHCO_3$ at 100 mV s^{-1} scan rate. **c**, Raman spectra of CoPc/CNT, CNT and CoPc. **d**, High-resolution STEM-HAADF image of CoPc/CNT. The high-contrast (white) dots are probably Co atoms. **e**,**f**, EDX spectrum of CoPc/CNT in comparison with that of bare CNTs.

DCA reduction to ethylene at −0.64 V, both based on the amount of EA CoPc on the electrode (Fig. 2c). If we normalize the reaction rate to the total mass of the CoPc/CNT catalyst, the $PR_{ethylene(TM)}$ value is 0.56 mmol $g^{-1}s^{-1}$ at −0.64 V, which is ~11 times higher with >1.3 V lower overpotential compared with the other catalysts reported to date (Fig. 2d and Supplementary Table 1). Considering that practical water treatment will need to process pollutants of various concentrations, we further investigated the electrocatalytic dechlorination reactivity of CoPc/CNT with varied DCA concentrations. High $FE_{ethylene}$ (>90%) is achieved throughout the concentration range from 87.0 to 8.7 mM (Fig. 2e).

To scrutinize the catalytic reaction pathway, we conducted electrochemical kinetic studies. First, the kinetic isotope effect (KIE) was measured with a $NaDCO_3/D_2O$ electrolyte compared with a normal $NaHCO_3/H_2O$ electrolyte[31]. In an Ar atmosphere, the HER current density (H_2 or D_2) is at least two times higher in the H electrolyte than that in the D electrolyte in the potential range of less than −0.74 V (Fig. 2f); this is consistent with the reaction mechanism that adsorbed hydrogen (*H or *D) or water (H_2O or D_2O) is involved in the RDS of the reaction[32,33]. In contrast, under DCA-saturated conditions, the current density in the potential range from −0.24 to −0.74 V, where the reduction of DCA to ethylene is dominant, does not change between the two electrolytes (Fig. 2f). At less than −0.84 V, the H electrolyte generates a larger current density than the D electrolyte as the HER becomes more dominant. These results suggest that the RDS of DCA electroreduction to ethylene and Cl^- does not involve *H. This mechanistic feature is also confirmed by electrochemical DCA dechlorination in the presence of *tert*-butanol (*t*-BuOH), which is known to chemically quench *H (ref. [34]). Having *t*-BuOH in the reaction media does not affect the partial current density or FE of DCA reduction to ethylene (Fig. 2g). Furthermore, DCA dechlorination in 0.1 M Na_2SO_4 or K_2SO_4 shows comparable performance to that in the $KHCO_3$ electrolyte on the standard hydrogen electrode (SHE) potential scale (Supplementary Fig. 9), another piece of evidence that the RDS of the reaction has no proton dependence. The absence of *H participating in the RDS of DCA electroreduction catalysed by CoPc/CNT, which is different from some electrochemical dechlorination reactions over metal catalysts[19,34,35], is a direct result of the single-site character of the heterogeneous molecular catalyst, as well as a key factor to enable selective DCA dechlorination in pH-neutral aqueous media and suppressing HER.

We also performed Tafel analysis for CoPc/CNT-catalysed electrochemical reduction of DCA to ethylene (Supplementary Fig. 10). A Tafel slope of ~60 mV dec^{-1} is observed in the potential range from −0.26 to −0.30 V (Fig. 2h), which indicates a rate-determining chemical reaction step following a one-electron transfer step if we assume a charge transfer coefficient of 0.5 for the electron transfer step[33]. The slope becomes greater than 118 mV dec^{-1} at more negative potentials as diffusion limitation starts to prevail at higher DCA consumption rates[33]. Considering that the overall DCA dechlorination reaction involves the addition of two electrons and the removal of two Cl^- (Supplementary Fig. 11), we postulate—on the basis of deuterium KIE, *H quenching and Tafel analysis results—that the chemical adsorption of DCA on the CoPc site proceeds via fast electron transfer from the catalyst to the reactant,

https://doi.org/10.1038/s41565-022-01277-z

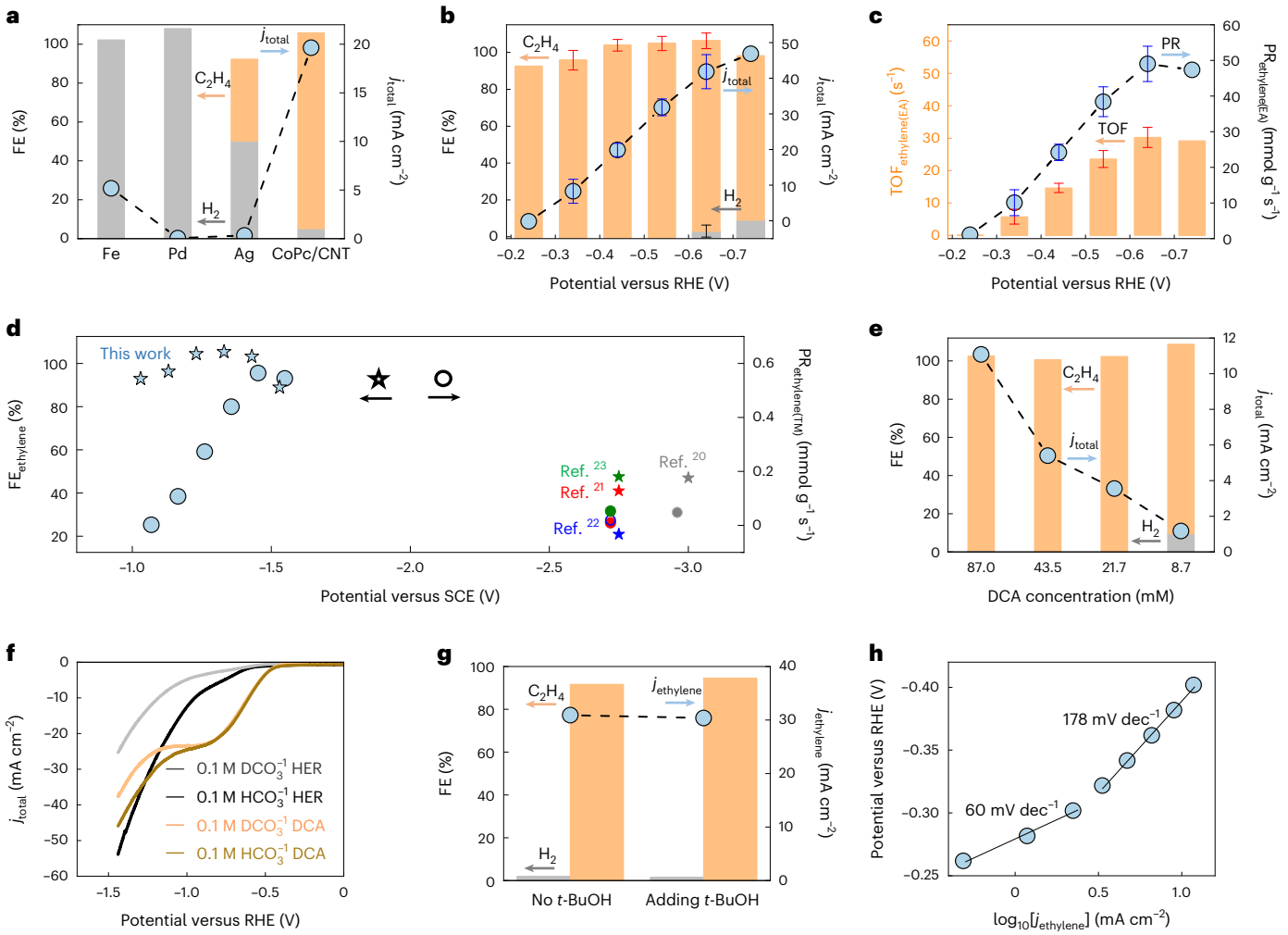

Fig. 2 | Electrocatalytic properties for DCA dechlorination measured in 0.1 M aqueous $KHCO_3$ saturated with DCA (~87 mM). a, Electrocatalytic dechlorination performance (FE and total current density j_{total}) of CoPc/CNT compared with Fe, Pd and Ag electrodes measured at −0.64 V versus RHE without stirring. **b**, Electrochemical dechlorination performance of CoPc/CNT with varied electrode potentials. The error bars represent standard deviations from three independent measurements. **c**, Potential-dependent TOF and PR of DCA reduction to ethylene catalysed by CoPc/CNT. $PR_{ethylene(EA)}$ is normalized to the mass of EA CoPc. The error bars represent standard deviations from three independent measurements. **d**, Comparison of DCA dechlorination selectivity ($FE_{ethylene}$) and reaction rate ($PR_{ethylene}$) of CoPc/CNT with other catalysts in the literature. $PR_{ethylene(TM)}$ is normalized to the total mass of the CoPc/CNT catalyst. **e**, Electrochemical dechlorination performance of CoPc/CNT with varied DCA concentrations at −0.64 V. **f**, KIE of CoPc/CNT for DCA dechlorination and HER measured in $NaDCO_3/D_2O$ versus $NaHCO_3/H_2O$ electrolyte. **g**, Electrochemical dechlorination performance of CoPc/CNT measured at −0.54 V with and without adding *t*-BuOH (~23 mg) to the electrolyte. **h**, Tafel slopes for the electrochemical dechlorination of DCA catalysed by CoPc/CNT. Electrochemical data are taken with stirring at 600 rpm, unless otherwise stated.

which is followed by a slow chemical step to remove Cl^- without the participation of *H.

Computational modelling

We performed DFT calculations to gain further insights into the catalytic mechanism. We selected CoPc/graphene as a model system (Fig. 3a) for our calculations. Considering the large diameter of our CNTs (~20 nm) and the much smaller size of the CoPc molecule (~1 nm), we believe that the curvature effect of the CNT structure is negligible in this case[36,37]. Indeed, we find that CoPc molecules supported on chemically derived graphene show similar selectivity, activity and Tafel slopes as the CoPc/CNT catalyst (Supplementary Fig. 12). The CoPc molecule is adsorbed with its aromatic plane parallel to graphene in a vertical distance of 3.28 Å. We predict an adsorption energy of −2.04 eV for CoPc on graphene. The Co centre of the CoPc molecule strongly interacts with the graphene support. The partial density of states plot (Fig. 3b) and crystal orbital Hamilton population analysis (Supplementary Fig. 13) show strong bonding of the C atoms of graphene with the e_g orbitals of the Co centre at −0.41 eV below the Fermi level. The adsorption of CoPc on graphene is accompanied by the transfer of 0.4e$^-$ from graphene to the CoPc molecule, which reduces the magnetic moment of Co by filling its d_{z^2} orbital (Supplementary Figs. 13 and 14).

Grand canonical quantum mechanics (GCQM) calculations[38] were performed for the DCA dechlorination reaction under an applied potential to analyse the reaction energetics. Based on the aforementioned KIE, *H quenching and Tafel slope results, we excluded the hydrodechlorination pathway[20,21]. Therefore, the DCA-to-ethylene conversion comprises two electron-coupled dechlorination steps, with the first forming adsorbed chloroethyl (*C_2H_4Cl) and the second yielding the ethylene product (Supplementary Fig. 11). Our calculations show that the free-energy change in the second dechlorination is much more favourable than that of the first dechlorination (Fig. 3c and Supplementary Fig. 15). This indicates that the first dechlorination

https://doi.org/10.1038/s41565-022-01277-z

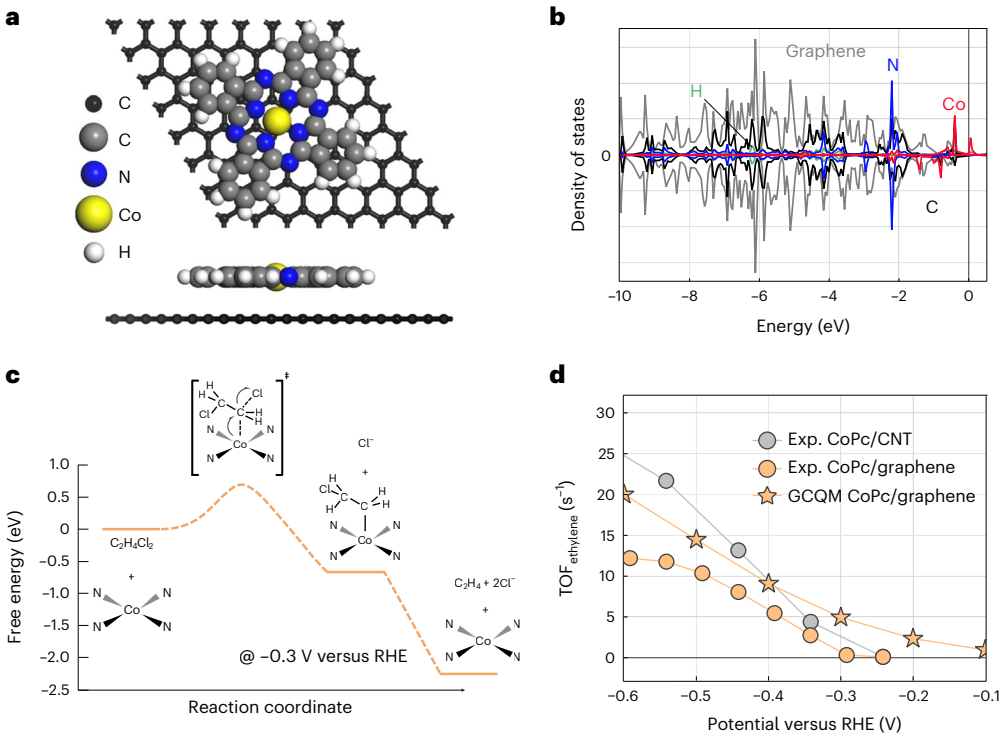

Fig. 3 | Calculated reaction pathway of electrochemical DCA dechlorination catalysed by CoPc. a, Geometric configuration of the CoPc/graphene model system. **b**, Local density of states of CoPc/graphene. **c**, Free-energy pathway of DCA reduction to ethylene. **d**, Comparison of GCQM-calculated TOF with the experimental results.

step dominates the kinetics, which is consistent with our experimental results. At the transition state of the first dechlorination step (Supplementary Fig. 16), the length of the breaking C–Cl bond is calculated to be 2.33 Å, which is 0.53 Å longer than the normal C–Cl bond in a free DCA molecule. The kinetic free-energy barrier of the first dechlorination step reduces from 0.78 eV to 0.68 eV as the potential decreases from 0 V to −0.6 V (Supplementary Fig. 15). This leads to TOFs of 4.9 s^{-1} at −0.3 V and 14.5 s^{-1} at −0.5 V at room temperature, which agrees well with the experimental results (Fig. 3d), and confirms the reaction mechanism that we deduced from our experiments. Consistent with the aforementioned experimental results (Supplementary Figs. 7 and 8), the calculations also suggest that the Co centre is the active site that binds the reaction intermediates. Other sites on the CoPc molecule, such as the N and C atoms, have a much higher energy barrier than the Co centre for the first dechlorination step (Supplementary Fig. 17), and are unlikely to be active sites.

Electrified membrane

We incorporated CoPc/CNT into an electrified membrane to investigate the feasibility of applying the catalyst for the treatment of DCA-contaminated water in a practical scalable flow-through operation mode. As shown by the schematic in Fig. 4a, the electrofiltration module contains a feed chamber with a RuO_2–IrO_2/Ti mesh electrode (top), a dimensionally stable anode commonly used for commercial applications and a permeate chamber with a ceramic membrane coated with CoPc/CNT (CoPc/CNT@CM) (bottom). The CoPc/CNT@CM membrane and RuO_2–IrO_2/Ti mesh serve as the cathode and anode, respectively (Supplementary Fig. 18). The feed solution consists of 0.5 mM (49 ppm) DCA in a 10 mM Na_2SO_4 aqueous electrolyte to simulate the halogenated pollutant concentration and ionic strength of environmentally relevant wastewater conditions. We selected the DCA concentration because it represents the DCA level in heavily polluted groundwater near landfills in the United States[1], and the Na_2SO_4 concentration because it is in the range of naturally occurring ionic strength and sulfate levels in environmental waters[39].

CoPc/CNT@CM was fabricated by vacuum filtering a CoPc/CNT suspension containing 0.1 wt% polyacrylonitrile (PAN) with a pristine CM substrate (Supplementary Fig. 19) to achieve a catalyst loading of 1 mg cm^{-2} (Supplementary Fig. 20). The 25-µm-thick CoPc/CNT layer on the membrane shows an interwoven structure with an average pore size of 15.1 nm (Fig. 4b,c and Supplementary Fig. 21), which can effectively facilitate the degradation/conversion of pollutants via convection-enhanced mass transport during the flow-through operation[40]. Due to the addition of PAN, CoPc/CNT@CM maintains a hydrophilic surface with a contact angle of 38.6° (Fig. 4d), which can mitigate membrane fouling. As a result of the compact catalyst layer, CoPc/CNT@CM exhibits a much lower water permeability of 62.6 l m^{-2} h^{-1} bar^{-1} compared with the CM substrate (592 l m^{-2} h^{-1} bar^{-1}) (Fig. 4e), which ensures a long residence time for the membrane to purify polluted water. Furthermore, CoPc/CNT@CM exhibits a two orders of magnitude smaller semicircle than the pristine CM substrate in the electrochemical impedance spectroscopy (EIS) measurements (Fig. 4f), demonstrating the high electrical conductivity of the CoPc/CNT active layer. These characteristics of the membrane optimize the operating conditions of the CoPc/CNT catalyst for DCA removal in the flow-through mode.

CoPc/CNT@CM shows superior DCA removal performance in single-pass electrofiltration tests with a residence time of ~3 s. A clear correlation is observed between the passed current density and DCA concentration in the permeate after 1 h (Fig. 4g and Supplementary Fig. 22). Specifically, 68% of the initial DCA is removed at 0.18 mA cm^{-2}. When the current density is increased to 0.74 mA cm^{-2}, a high removal efficiency of 96% is achieved with a low electrical energy consumption per order (E_{EO}) of 0.42 kWh m^{-3} for DCA (Fig. 4g). Based on the concentration of Cl^- in the permeate, 73% of the removed DCA is transformed to ethylene. The rest of the removed DCA is probably adsorbed in the

https://doi.org/10.1038/s41565-022-01277-z

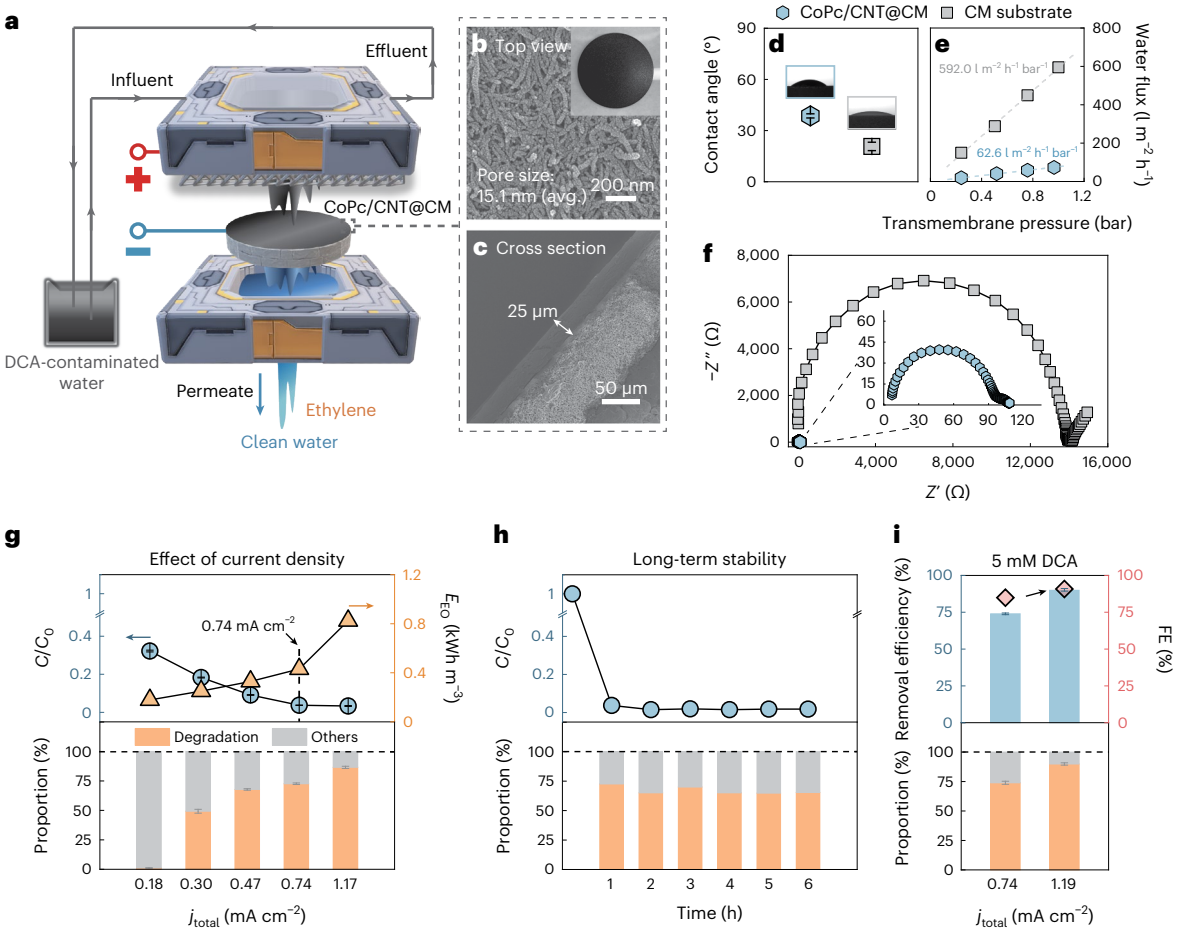

Fig. 4 | CoPc/CNT-functionalized electrochemical membrane for the treatment of DCA-contaminated water. a, Schematic of the cross-flow electrified membrane filtration system. **b**,**c**, Scanning electron microscopy images depicting the top and cross-sectional views of CoPc/CNT@CM. The inset in **b** is a photograph of CoPc/CNT@CM. **d**, Water contact angles of CoPc/CNT@CM and CM. **e**, Water flux of CoPc/CNT@CM and CM as a function of the transmembrane pressure. **f**, EIS spectra of CoPc/CNT@CM and CM over a frequency range of 1–10^6 Hz in 10 mM Na_2SO_4 solution at the open-circuit voltage. **g**, Effect of current density on DCA concentration change (top-left axis), E_{EO} (top-right axis) and DCA degradation proportion (bottom). The vertical dashed line in the top panel indicates the optimal current density, that is, 0.74 mA cm^{-2}, for DCA dechlorination using CoPc/CNT@CM. **h**, DCA concentration change (top) and DCA degradation proportion (bottom) as a function of operation time at 0.74 mA cm^{-2}. Electrofiltration experiments in **g** and **h** were conducted using a feed solution with 0.5 mM DCA and 10.0 mM Na_2SO_4. **i**, Effect of current density on DCA removal efficiency (top-left axis), FE (top-right axis) and DCA degradation proportion (bottom) using a feed solution with an increased initial DCA concentration of 5 mM. The error bars in **d**, **g** and **i** represent standard deviations from three independent measurements.

pores of CoPc/CNT@CM. Indeed, the CNT@CM membrane without CoPc can remove ~55% of DCA in single-pass filtration at 0.74 mA cm^{-2}, but only via adsorption (Supplementary Fig. 23). This confirms the role of CoPc as the catalytic centre in the CoPc/CNT@CM membrane for DCA degradation. Further increasing the current density marginally increases DCA removal to 97%, but considerably improves the degradation proportion to 90% with compromised energy efficiency (Fig. 4g). The increased DCA degradation proportion at higher current density demonstrates that the adsorbed DCA in the porous carbonaceous structure can be electrochemically decomposed, suggesting a synergistic effect of adsorption and electrodegradation in achieving the abovementioned high performance and energy efficiency for DCA treatment.

Flow-through electrofiltration can be continuously operated for 6 h until the feed solution is completely consumed. Near 100% DCA removal efficiency and high DCA degradation proportion are maintained throughout the operation (Fig. 4h and Supplementary Fig. 24), which reflects the durability of the CoPc/CNT@CM membrane for the purification of DCA-contaminated water. The membrane shows no compromise in performance when treating simulated surface water dosed with DCA (Supplementary Fig. 25 and Supplementary Table 2), demonstrating its suitability for practical wastewater treatment. We also conducted experiments with a higher initial DCA concentration of 5 mM to simulate high-load operating conditions. The electrified CoPc/CNT@CM membrane removes 96% of the DCA with 92% of the removal caused by electrochemical decomposition at an optimized current density of 1.19 mA cm^{-2} (Fig. 4i). Notably, electrons are efficiently used to reduce DCA, as evidenced by the high FE of 90%. These results demonstrate the potential of our CoPc/CNT@CM for the effective and efficient treatment of various DCA-contaminated environmental waters.

Conclusions

This study demonstrates the possibility to solve challenges present in the electrochemical treatment of chlorinated organic pollutants in water by developing better catalysis. Our CoPc/CNT catalyst exhibits near-unity FE and high reaction rates for electrochemical DCA decomposition into ethylene in aqueous solutions across wide electrode potential and DCA concentration ranges. Kinetic studies and DFT calculations reveal that the first dechlorination step is the RDS, which is

responsible for efficient DCA reduction and effective HER suppression on the catalyst. Incorporating CoPc/CNT into a flow-through electrified membrane demonstrates >95% DCA removal from simulated water samples with environmentally relevant DCA concentrations.

Online content

Any methods, additional references, Nature Portfolio reporting summaries, source data, extended data, supplementary information, acknowledgements, peer review information; details of author contributions and competing interests; and statements of data and code availability are available at https://doi.org/10.1038/s41565-022-01277-z.

References

1. Agency for Toxic Substances and Disease Registry. *Toxicological Profile for 1,2-Dichloroethane* (US Department of Health and Human Services, 2001); https://www.atsdr.cdc.gov/toxprofiles/tp38.pdf
2. Field, J. A. & Sierra-Alvare, R. Biodegradability of chlorinated solvents and related chlorinated aliphatic compounds. *Rev. Environ. Sci. Biotechnol.* **3**, 185–254 (2004).
3. American Chemistry Council. *2020 Guide to the Business of Chemistry* (2020); https://www.americanchemistry.com/content/download/3640/file/2020-Guide-to-the-Business-of-Chemistry.pdf
4. Sherwood, J. European restrictions on 1,2-dichloroethane: C–H activation research and development should be liberated and not limited. *Angew. Chem. Int. Ed.* **57**, 14286–14290 (2018).
5. Leow, D. et al. Activation of remote meta-C–H bonds assisted by an end-on template. *Nature* **486**, 518–522 (2012).
6. Wang, X. C. et al. Ligand-enabled meta-C–H activation using a transient mediator. *Nature* **519**, 334–338 (2015).
7. Phipps, R. J. & Gaunt, M. J. A meta-selective copper-catalyzed C–H bond arylation. *Science* **323**, 1593–1597 (2009).
8. *The 2019 Toxics Release Inventory (TRI) National Analysis* (United States Environmental Protection Agency, 2019); https://www.epa.gov/trinationalanalysis/releases-chemical-and-industry
9. *National Primary Drinking Water Regulations* (United States Environmental Protection Agency, 2009); https://www.epa.gov/sites/default/files/2016-06/documents/npwdr_complete_table.pdf
10. Vogel, T. et al. ES&T critical reviews: transformations of halogenated aliphatic compounds. *Environ. Sci. Technol.* **21**, 722–736 (1987).
11. Capel, P. D. & Larson, S. J. A chemodynamic approach for estimating losses of target organic chemicals from water during sample holding time. *Chemosphere* **30**, 1097–1107 (1995).
12. van der Zaan, B. et al. Degradation of 1,2-dichloroethane by microbial communities from river sediment at various redox conditions. *Water Res.* **43**, 3207–3216 (2009).
13. De Luna, P. et al. What would it take for renewably powered electrosynthesis to displace petrochemical processes? *Science* **364**, eaav3506 (2019).
14. Williams, C. K. et al. Electrocatalytic dechlorination of dichloromethane in water using a heterogenized molecular copper complex. *Inorg. Chem.* **60**, 4915–4923 (2021).
15. Williams, C. K. et al. Hydrodechlorination of dichloromethane by a metal-free triazole-porphyrin electrocatalyst: demonstration of main-group element electrocatalysis. *Chem. Eur. J.* **27**, 6240–6246 (2021).
16. Scialdone, O. et al. Electrochemical abatement of chloroethanes in water: reduction, oxidation and combined processes. *Electrochim. Acta* **55**, 701–708 (2010).
17. Scialdone, O. et al. Electrochemical incineration of 1,2-dichloroethane: effect of the electrode material. *Electrochim. Acta* **53**, 7220–7225 (2008).
18. Sonoyama, N. & Sakata, T. Electrochemical continuous decomposition of chloroform and other volatile chlorinated hydrocarbons in water using a column type metal impregnated carbon fiber electrode. *Environ. Sci. Technol.* **33**, 3438–3442 (1999).
19. Hori, Y. et al. Electrochemical dechlorination of chlorinated hydrocarbons—electrochemical reduction of chloroform in acetonitrile/water mixtures at high current density. *Chem. Lett.* **32**, 230–231 (2003).
20. Gan, G. et al. Active sites in single-atom Fe–N_x–C nanosheets for selective electrochemical dechlorination of 1,2-dichloroethane to ethylene. *ACS Nano* **14**, 9929–9937 (2020).
21. Xu, F. et al. Manganese-based spinel core–shell nanostructures for efficient electrocatalysis of 1,2-dichloroethane. *ACS Appl. Nano Mater.* **3**, 10778–10786 (2020).
22. Gan, G. et al. Identification of catalytic active sites in nitrogen-doped carbon for electrocatalytic dechlorination of 1,2-dichloroethane. *ACS Catal.* **9**, 10931–10939 (2019).
23. Gan, G. et al. Nature of intrinsic defects in carbon materials for electrochemical dechlorination of 1,2-dichloroethane to ethylene. *ACS Catal.* **11**, 14284–14292 (2021).
24. Wu, Y. et al. Domino electroreduction of CO_2 to methanol on a molecular catalyst. *Nature* **575**, 639–642 (2019).
25. Zhang, X. et al. Highly selective and active CO_2 reduction electrocatalysts based on cobalt phthalocyanine/carbon nanotube hybrid structures. *Nat. Commun.* **8**, 14675 (2017).
26. Wang, H. et al. An ultrafast nickel–iron battery from strongly coupled inorganic nanoparticle/nanocarbon hybrid materials. *Nat. Commun.* **3**, 917 (2012).
27. Yueshen, W. et al. Direct electrosynthesis of methylamine from carbon dioxide and nitrate. *Nat. Sustain.* **4**, 725–730 (2021).
28. Wu, Y. et al. Graphene-veiled gold substrate for surface-enhanced Raman spectroscopy. *Adv. Mater.* **25**, 928–933 (2013).
29. Esenpınar, A. A. et al. Synthesis and electrochemistry of tetrakis (7-coumarinthio-4-methyl)-phthalocyanines, and preparation of their cinnamic acid and sodium cinnamate derivatives. *Polyhedron* **28**, 33–42 (2009).
30. Akyüz, D. et al. Metallophthalocyanines bearing polymerizable {[5-({(1E)-[4-(diethylamino)phenyl]methylene}amino)-1-naphthyl] oxy} groups as electrochemical pesticide sensor. *Electroanalysis* **29**, 2913–2924 (2017).
31. Wiberg, K. B. The deuterium isotope effect. *Chem. Rev.* **55**, 713–743 (1955).
32. Kahyarian, A. et al. Mechanism of the hydrogen evolution reaction in mildly acidic environments on gold. *J. Electrochem. Soc.* **164**, H365 (2017).
33. Fang, Y. H. et al. Tafel kinetics of electrocatalytic reactions: from experiment to first-principles. *ACS Catal.* **4**, 4364–4376 (2014).
34. Huang, D. et al. Elucidating the role of single-atom Pd for electrocatalytic hydrodechlorination. *Environ. Sci. Technol.* **55**, 13306–13316 (2021).
35. Mao, X. et al. Redox control for electrochemical dechlorination of trichloroethylene in bicarbonate aqueous media. *Environ. Sci. Technol.* **45**, 6517–6523 (2011).
36. Hernandez, E. et al. Elastic properties of C and $B_xC_yN_z$ composite nanotubes. *Phy. Rev. Lett.* **80**, 4502–4505 (1998).
37. Guanghua, G. et al. Energetics, structure, mechanical and vibrational properties of single-walled carbon nanotubes. *Nanotechnology* **9**, 184–191 (1998).
38. Huang, Y. et al. Reaction mechanism for the hydrogen evolution reaction on the basal plane sulfur vacancy site of MoS_2 using grand canonical potential kinetics. *J. Am. Chem. Soc.* **140**, 16773–16782 (2018).

39. *Drinking Water Advisory: Consumer Acceptability Advice and Health Effects Analysis on Sulfate* (United States Environmental Protection, 2003); http://www.epa.gov/safewater/ccl/pdf/sulfate.pdf
40. Sun, M. et al. Electrified membranes for water treatment applications. *ACS EST Engg.* **1**, 725–752 (2021).

Methods

Materials

DCA (anhydrous, 99.8%), *N*,*N*-dimethylformamide (DMF; anhydrous, 99.8%), PAN (M_w, 150,000; quality level, 200), cobalt(II) phthalocyanine (CoPc), $KHCO_3$ (99.7%) and Na_2SO_4 (99.7%) were purchased from Sigma-Aldrich. K_2SO_4 (99%) was purchased from Alfa Aesar. Multiwalled CNTs were purchased from C-Nano (product no. FT 9100). Ar (99.999%) was purchased from Airgas. Deionized water (18.2 MΩ cm at 25 °C) from a Millipore water purification system was used throughout the experiments. Unless otherwise noted, all the commercial chemicals were used without purification.

Characterization

ICP-MS was conducted with an Agilent Technologies 7700 series or PerkinElmer NexION 5000 instrument. A Bruker 400M nuclear magnetic resonance (NMR) instrument was used to record ^{1}H NMR. We used a gas chromatograph (MG#5, SRI Instruments) equipped with a flame ionization detector and a thermal conductivity detector to analyse the gas products of electrocatalysis. STEM imaging and EDX mapping were performed using a dual-Cs-corrected FEI Themis G2 microscope at 60 kV with a Super-X EDS detector. High-resolution STEM-HAADF images were acquired with a Cs-probe-corrected Thermo Fisher Scientific Spectra 300 Kraken (S)TEM with an extreme-brightness cold field emission gun. Data were collected at 120 kV with a probe current of ~60 pA. A Raman microscope (LabRAM HR Evolution, Horiba Jobin Yvon) with a 633 nm laser was used for collecting the Raman spectra. CoPc/CNT was deposited on a titanium foil coated with 20 nm gold for surface-enhanced Raman scattering. X-ray photoelectron spectroscopy was performed on a PHI VersaProbe II X-ray photoelectron spectrometer with an Al K_α target (1,486.7 eV).

Preparation of CoPc/CNT and CoPc/graphene

We first calcined as-received CNTs at 500 °C in air for 5 h. The calcined CNTs were sonicated in a 5 wt% HCl aqueous solution for 30 min, followed by stirring overnight. Then, the CNTs were washed with deionized water until pH neutral and collected by freeze drying to yield purified CNTs. Then, 30.0 mg of purified CNTs in 30 ml DMF and 1.5 mg CoPc in 15 ml DMF were separately prepared, and each was sonicated for 1 h to achieve a well-dispersed CNT suspension and a fully dissolved CoPc solution, respectively. Then, the two solutions were merged and sonicated for 1 h followed by stirring at room temperature for 20 h. Subsequently, the solution was centrifuged, and the supernatant was discarded. The precipitate was washed with DMF and centrifuged twice until the supernatant was colourless. Finally, the product was washed with deionized water and centrifuged twice before it was freeze dried to yield CoPc/CNT (ref. [24]). ICP-MS measurements confirmed the weight percentage of Co in the hybrid material to be ~2.6%. The preparation of CoPc/graphene followed the same procedure except that reduced graphene oxide was used in the place of CNTs. Graphene oxide was prepared following prior work[41,42]. Lyophilized graphene oxide was reduced to graphene at 600 °C in a mixed gas atmosphere (10 standard cubic centimetres per minute (s.c.c.m.) H_2 and 190 s.c.c.m. Ar) for 2 h.

Preparation of electrolyte solutions

Purification of 0.1 M $KHCO_3$, K_2SO_4 or Na_2SO_4 aqueous electrolyte solutions (500 ml) was conducted with a two-electrode setup using two 99.99% Ti foil electrodes (10 × 5 cm^2). The purification was conducted with stirring at 2.5 V until the current decreased to 150 μA, and the current was then maintained at 150 μA for 24 h. At the end of the purification, the Ti electrodes were removed from the solution before the applied potential was released to avoid the electrodeposited impurities from re-entering the solution.

Preparation of electrodes

Here 2 mg of CoPc/CNT (or other catalyst materials tested in this work) in 1 ml of ethanol with 10 μl of a 5 wt% Nafion solution (Sigma-Aldrich) was sonicated for 1 h to prepare a catalyst ink. Then, 100 μl of this ink was drop casted on a 3.0 × 0.5 cm^2 polytetrafluoroethylene-treated carbon fibre paper (Toray 030, Fuel Cell Store) and dried under an infrared lamp. The covered geometric area was 0.5 × 1.0 cm^2, giving a catalyst mass loading of 0.4 mg cm^{-2}. The Ag, Fe and Pd electrodes for comparison were prepared by sputter coating (Leica ACE 600 Sputter Coater) 50 nm of the corresponding metal on a carbon-fibre-paper substrate. The covered geometric area was 1 × 1 cm^2.

Electrochemical measurements

Electrochemical DCA dechlorination was carried out in purified 0.1 M $KHCO_3$ at room temperature and atmospheric pressure with a custom-designed gas-tight H cell (12 g of electrolyte and ~18 ml of gas headspace for each compartment). Ar was flown at 20 s.c.c.m. through a pure DCA liquid to carry DCA vapour into the cathode compartment for at least 20 min before electrolysis. Ar with DCA vapour was kept bubbling into the electrolyte during electrolysis, unless otherwise noted (the electrolyte was saturated by DCA with a concentration of ~87 mM). A graphite rod from Sigma-Aldrich was used as the counter electrode, and Ag/AgCl (0.1976 V versus SHE) electrode from Pine Research Instrumentation was used as the reference electrode. An anion-exchange membrane (Selemion DSV) separated the cathode and anode compartments. A Bio-Logic VMP3 multi-potentiostat was used for all the electrochemical experiments. EIS measurements were conducted to determine the ohmic drop between the working electrode and reference electrode at −0.5 V versus Ag/AgCl between 200 kHz and 1 Hz with an amplitude of 10 mV. In the Nyquist plot, the curve's intersection with the real axis was collected as the resistance, which was automatically corrected with 100% iR compensation during all the electrochemical measurements. The current was normalized to the catalyst-covered geometric area. We converted all the recorded potentials (V) to the RHE scale with the following formula (unless otherwise stated): $V_{RHE} = V_{Ag/AgCl} + (0.1976\ V) + (0.0592\ V) \times pH$. All the electrochemical DCA dechlorination measurements were conducted with stirring at 600 rpm, unless otherwise noted.

KIE

Then, 0.10 M $NaDCO_3$ and 0.10 M $NaHCO_3$ aqueous solutions were prepared by bubbling CO_2 gas through 0.05 M Na_2CO_3 in D_2O and 0.05 M Na_2CO_3 in H_2O for at least 6 h, respectively. For DCA dechlorination, 20 s.c.c.m. Ar carrying DCA vapour was bubbled in the cathode compartment for at least 4 h. For HER, pure Ar was purged for 4 h. Cyclic voltammetry was conducted at 50 mV s^{-1} scan rate with 600 rpm stirring.

$TOF_{ethylene}$ and $PR_{ethylene}$ calculations

$TOF_{ethylene(EA)}$ was reported as the mole number of ethylene produced per mole number of EA CoPc per second. EA CoPc was calculated by integrating the one-electron oxidation peak at ~0.185 V versus RHE. $PR_{ethylene(EA)}$ was reported as the mole number of ethylene produced per gram of EA CoPc per second. The total mass of the CoPc/CNT catalyst was used to calculate $PR_{ethylene(TM)}$.

*H quenching with *t*-BuOH

Electrochemical dechlorination with CoPc/CNT was carried out at −0.54 V versus RHE for 15 min. Then, ~23 mg of *t*-BuOH was injected into the $KHCO_3$ electrolyte (corresponding to a *t*-BuOH concentration of ~25 mM) using a syringe without interrupting the electrolysis. The effect of adding *t*-BuOH on the electrocatalytic performance was recorded.

Co-leaching test

After 30 min of DCA dechlorination catalysed by CoPc/CNT at −0.54 V versus RHE, 1.17 g of the 0.1 M $KHCO_3$ electrolyte was collected from the cathode compartment. The collected electrolyte sample was mixed with 12 ml of trace-metal-basis 1% HNO_3 for ICP-MS measurements.

Electrocatalysis with varied DCA concentrations

Here ~87 mM DCA in purified 0.1 M $KHCO_3$ aqueous electrolyte was prepared by saturating the solution with DCA bubbling. The DCA-saturated electrolyte was then diluted with purified 0.1 M $KHCO_3$ electrolyte to prepare the electrolyte solutions containing 43.5 mM, 21.7 mM and 8.7 mM DCA. Electrochemical dechlorination with CoPc/CNT was conducted at −0.64 V versus RHE with stirring at 600 rpm in the prepared electrolyte under Ar purging (20 s.c.c.m.) for 10 min. The exit gas was analysed by the gas chromatograph.

Product quantification

The exit gas tubing of the electrolyser was connected to an SRI Multiple Gas Analyser #5 gas chromatography system with a flame ionization detector and a thermal conductivity detector. High-purity Ar was used as the carrier gas. Calibration curves, which were made by diluting a standard gas with CO_2 to different concentrations through a mass flow controller, were used to convert the peak areas of the products (H_2 and C_2H_4) to gas volumes. DCA concentration was quantified by using ^{1}H NMR spectroscopy with water suppression. NMR samples were prepared by mixing 450 µl of electrolyte with 50 µl of 10 mM dimethyl sulfoxide in D_2O (99.9 at.%; Sigma-Aldrich) as an the internal standard. The areal ratio of the DCA peak to the dimethyl sulfoxide peak was used to determine the DCA concentration.

Preparation of CoPc/CNT@CM

CoPc/CNT was dispersed in a PAN solution (0.1 wt% in DMF) at 2 mg ml^{-1} followed by sonication using an ultrasonic probe to obtain a CoPc/CNT suspension. CoPc/CNT@CM with a material loading of 1 mg cm^{-2} was fabricated by vacuum filtration of the as-prepared CoPc/CNT suspension onto a pristine CM substrate (Sterlitech), as illustrated by the schematic in Supplementary Fig. 20. The membrane was then rinsed with deionized water followed by drying at 90 °C for 12 h. CoPc/CNT@CM had an effective area of 12.6 cm^2. CNT@CM with the same material loading was also prepared through the above method for comparison.

Membrane characterization

The surface and cross-sectional morphology of CoPc/CNT@CM was investigated using a scanning electron microscope (SU8230, Hitachi). Surface scanning electron microscopy images were analysed by the Nano Measurer 1.2 software to estimate the pore size distribution of the membrane. The water contact angle was measured by the sessile drop method using a contact angle goniometer (OneAttension, Biolin Scientific). The water flux was calculated by dividing the permeate volume by the effective membrane area and interval time. Membrane pore volume was determined by the weight difference between a wet and dry membrane, and the retention time of water within the membrane was calculated based on the pore volume and water flux. The EIS data of the membrane were measured by an electrochemical workstation (CHI 660E, CH Instruments) in a typical three-electrode electrochemical cell, containing the tested membrane as the working electrode, mixed metal oxide (RuO_2–IrO_2/Ti) mesh as the counter electrode and Ag/AgCl electrode as the reference electrode. EIS was conducted by applying a frequency ranging from 1 to 10^6 Hz in 10 mM Na_2SO_4 solution at the open-circuit voltage.

Electrofiltration procedure

Electrofiltration experiments were performed using a cross-flow membrane filtration system. The electrofiltration module comprised a feed chamber with a RuO_2–IrO_2/Ti mesh and a permeate chamber (Supplementary Fig. 8). CoPc/CNT@CM and the RuO_2–IrO_2/Ti mesh serving as the cathode and anode, respectively, were connected by a d.c. power supply (E3646A, Agilent). The feed solution (500 ml) was circulated at a flow rate of 200 ml min^{-1} by a peristaltic pump (Masterflex, Cole-Parmer) and a transmembrane pressure of 11 psi was applied to obtain a permeate flow rate of 1 ml min^{-1} (corresponding to a water residence time of ~3 s in the membrane active layer). This filtration rate accelerated the mass transport rate because of convection-enhanced mass transport. After 1 h of operation (unless otherwise stated), DCA and Cl^- concentrations in both feed and permeate were quantified. DCA quantification was done by ^{1}H NMR, and Cl^- was measured by an adapted mercury(II) thiocyanate method using an assay kit (HI93753, Hanna Instruments). The experiments were also conducted without inserting the membrane to determine the amount of unexpected DCA loss. DCA degradation proportion was estimated based on Cl^- generation in the membrane filtration experiments. Energy consumption per order, E_{EO}, for DCA removal during filtration was evaluated using

$$E_{EO} = \frac{U_{cell} I}{Q \log\left[\frac{C_0}{C}\right]},$$

where U_{cell} and I are the applied voltage and current, respectively; Q is the permeate flow rate; and C_0 and C are the DCA concentrations before and after treatment, respectively.

Computational details

Our model system employed a graphene sheet (98 C atoms) and a CoPc molecule on top of the graphene with a 15 Å vacuum between them. The Vienna ab initio simulation package (version 5.4.5)[43,44] with the VASPsol solvation model[45] was used for geometry optimization followed by single-point calculations as a function of applied potential using the CANDLE solvation model[46] as incorporated in the joint density functional theory (JDFTx)[47]. Electron exchange and correlation were treated within the generalized gradient approximation[48] in the form of the Perdew–Burke–Ernzerhof functional, including the D3 correction for London dispersion (van der Waals attraction)[49]. The interaction between the ionic core and valence electrons was described by the projector-augmented-wave method[50]. We used a plane-wave basis set with an energy cutoff of 500 eV. The Brillouin zone was sampled using a 3 × 3 × 1 Monkhorst–Pack grid[51] for the electronic structure of CoPc/graphene. The convergence criteria for the electronic structure and atomic geometry were 10^{-5} eV and 0.03 eV Å^{-1}. For transition-state searching, we used the climbing-image nudged elastic band method[52], and we fixed the atomic positions of the graphene substrate and benzene rings in CoPc for better convergence. For JDFTx single-point calculations, we used the GBRV[53] ultrasoft pseudopotential with a plane-wave cutoff of 544 eV (20 Hartree). The ionic screening of different net charges was achieved with 0.1 M K^+ and 0.1 M F^- in the fluid model. All the other settings were similar to those in the Vienna ab initio simulation package calculations.

The Gibbs free energy (G) of all the surface states at 298 K and 1 atm was calculated as

$$G = H - T\Delta S = E_{DFT} + E_{ZPE} + E_{solv} + \int_0^{298} C_v \mathrm{d}T - T\Delta S,$$

where E_{DFT} is the electronic total energy, E_{ZPE} is the zero-point vibrational energy and E_{solv} is the solvation energy. The enthalpy ($\int_0^{298} C_v \mathrm{d}T$) and entropy ($\Delta S$) contributions at room temperature were calculated from the vibrational modes of the system. The grand canonical free energies (H) were obtained for all the states using the grand canonical potential method[38] to describe the effect of applied potential to the substrate and adsorbates.

The chemical potential of the dissolved DCA in the aqueous electrolyte ($\mu_{DCA_{(aq)}}$) was calculated as follows:

$$\mu_{DCA_{(aq)}} = E_{DFT}^{DCA_{(g)}} + ZPE_{DCA_{(g)}} - TS^0_{DCA_{(g)}} + \Delta G^{sol}_{DCA} + k_B T \ln(a^{DCA}),$$

where $E_{DFT}^{DCA_{(g)}}$ is the electronic total energy from JDFTx, $ZPE_{DCA_{(g)}}$ and $TS^0_{DCA_{(g)}}$ are the zero-point energy (ZPE) and entropy contribution of an ideal gas-phase DCA molecule using the Jaguar code[54], ΔG^{sol}_{DCA} is the

solvation free energy of DCA (2.49 kcal mol^{-1}) from experiment[55], k_B is the Boltzmann constant, T is the room temperature (298 K) and a^{DCA} is the concentration of DCA in our electrolyte (87 mM).

The chemical potential of the chloride anion in the aqueous electrolyte ($\mu_{Cl^-_{(aq)}}$) was calculated as follows:

$\mu_{Cl^-_{(aq)}} = E^{Cl^{\cdot}_{(g)}}_{DFT} - TS^{0}_{Cl^{\cdot}_{(g)}} + EA_{Cl^{\cdot}_{(g)}} + \Delta G^{sol}_{Cl^-_{(g)}}$, where $E^{Cl^{\cdot}_{(g)}}_{DFT}$ is the electronic total energy of a gas-phase chlorine radical from JDFTx, $TS^{0}_{Cl^{\cdot}_{(g)}}$ is the entropy contribution of the ideal gas-phase chlorine radical obtained using the Jaguar code, $EA_{Cl^{\cdot}_{(g)}}$ is the electron affinity of gas-phase chlorine radical (3.614 eV) from experiment[56] and $\Delta G^{sol}_{Cl^-_{(g)}}$ is the solvation free energy of chloride anion (−74.5 kcal mol^{-1}) from experiment[57].

Data availability

The atomic coordinates of the optimized structures (at neutral charge) for DFT calculations are provided in Supplementary Data 1. The measurement data presented within this paper and other findings of this study are available from the corresponding authors upon reasonable request.

References

41. Shahriary, L. et al. Graphene oxide synthesized by using modified Hummers approach. *Int. J. Renew. Energy Environ. Eng.* **2**, 58–63 (2014).
42. An, S. et al. A graphene oxide cookbook: exploring chemical and colloidal properties as a function of synthesis parameters. *J. Colloid Interface Sci.* **588**, 725–736 (2021).
43. Kresse, G. & Hafner, J. Ab initio molecular-dynamics simulation of the liquid-metal–amorphous-semiconductor transition in germanium. *Phys. Rev. B* **49**, 14251–14269 (1994).
44. Kresse, G. & Furthmüller, J. Efficient iterative schemes for ab initio total-energy calculations using a plane-wave basis set. *Phys. Rev. B* **54**, 11169–11186 (1996).
45. Mathew, K. et al. Implicit solvation model for density-functional study of nanocrystal surfaces and reaction pathways. *J. Chem. Phys.* **140**, 084106 (2014).
46. Sundararaman, R. & Goddard, W. A. III The charge-asymmetric nonlocally determined local-electric (CANDLE) solvation model. *J. Chem. Phys.* **142**, 064107 (2015).
47. Sundararaman, R. et al. JDFTx: software for joint density-functional theory. *SoftwareX* **6**, 278–284 (2017).
48. Perdew, J. P. et al. Generalized gradient approximation made simple. *Phys. Rev. Lett.* **77**, 3865–3868 (1996).
49. Johnson, E. R. & Becke, A. D. A post-Hartree-Fock model of intermolecular interactions: Inclusion of higher-order corrections. *J. Chem. Phys.* **124**, 174104 (2006).
50. Blöchl, P. E. Projector augmented-wave method. *Phys. Rev. B* **50**, 17953–17979 (1994).
51. Monkhorst, H. J. & Pack, J. D. Special points for Brillouin-zone integrations. *Phys. Rev. B* **13**, 5188–5192 (1976).
52. Henkelman, G. et al. A climbing image nudged elastic band method for finding saddle points and minimum energy paths. *J. Chem. Phys.* **113**, 9901–9904 (2000).
53. Garrity, K. F. et al. Pseudopotentials for high-throughput DFT calculations. *Comput. Mater. Sci.* **81**, 446–452 (2014).
54. Bochevarov, A. D. et al. Jaguar: a high-performance quantum chemistry software program with strengths in life and materials sciences. *Int. J. Quantum Chem.* **113**, 2110–2142 (2013).
55. Abraham, M. H. et al. Thermodynamics of solute transfer from water to hexadecane. *J. Chem. Soc., Perkin Trans.* **2**, 291–300 (1990).
56. Berzinsh, U. et al. Isotope shift in the electron affinity of chlorine. *Phys. Rev. A* **51**, 231–238 (1995).
57. Kelly, C. P. et al. Single-ion solvation free energies and the normal hydrogen electrode potential in methanol, acetonitrile, and dimethyl sulfoxide. *J. Phys. Chem. B* **111**, 408–422 (2007).

Acknowledgements

This work (materials synthesis, structural characterization and catalysis work) was primarily supported as part of the Center for Hybrid Approaches in Solar Energy to Liquid Fuels (CHASE), an Energy Innovation Hub funded by the US Department of Energy, Office of Science, Office of Basic Energy Sciences, under award no. DE-SC0021173 (H.W.). Computational work was supported by the Liquid Sunlight Alliance, which is supported by the US Department of Energy, Office of Science, Office of Basic Energy Sciences, Fuels from Sunlight Hub under award no. DE-SC0021266 (W.A.G.) and an individual fellowship from the Resnick Sustainability Institute at Caltech (S.K.), and used the Extreme Science and Engineering Discovery Environment (XSEDE) for DFT calculations, which is supported by National Science Foundation grant no. ACI-1548562 (W.A.G.). Electrified membrane filtration work was supported by the NSF Nanosystems Engineering Research Center for Nanotechnology-Enabled Water Treatment (EEC-1449500; M.E.). STEM and EDX characterizations were supported by the NSF career award no. 1749742 (J.J.C.). We thank J. Lee and J. D. Fortner (Department of Chemical and Environmental Engineering, Yale University) for providing graphene oxide.

Author contributions

C.C. and H.W. conceived and designed the project. C.C. and C.L.R. prepared the CoPc/CNT. C.C. conducted the electrocatalytic DCA dechlorination. X.W. conducted the flow-through DCA dechlorination with supervision from M.E. S.K. carried out the DFT calculations with supervision from W.A.G. J.L.H. and Q.P.S. performed the TEM imaging with supervision from J.J.C. N.J.H. performed the ICP-MS measurements. C.C. and H.W. wrote the manuscript with input from X.W. and S.K. H.W. supervised the project. All the authors discussed the results and commented on the manuscript.

Competing interests

The authors declare no competing interests.

Additional information

Supplementary information The online version contains supplementary material available at https://doi.org/10.1038/s41565-022-01277-z.

Correspondence and requests for materials should be addressed to William A. Goddard, Menachem Elimelech or Hailiang Wang.

Peer review information *Nature Nanotechnology* thanks Guohua Chen and the other, anonymous, reviewer(s) for their contribution to the peer review of this work.